nature nanotechnology

Supplementary information

https://doi.org/10.1038/s41565-026-02227-9

Self-assembled contacts for high-yield molecular devices

In the format provided by the authors and unedited

TABLE OF CONTENTS

SUPPLEMENTARY FIGURES

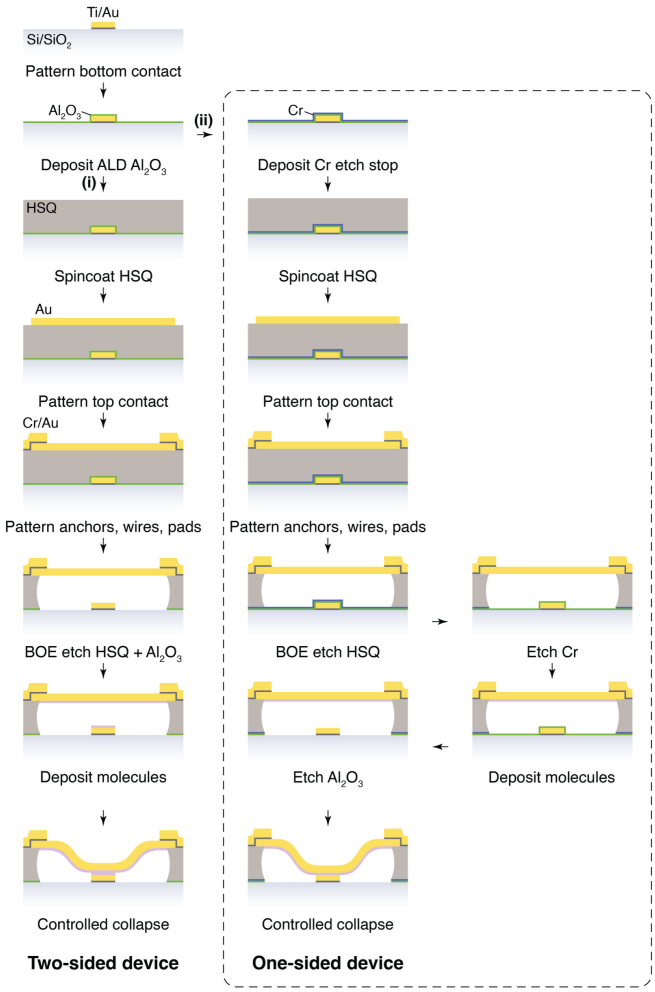

Supplementary Fig. 1 | Self-assembled contacts fabrication flow. First, the device scaffold is fabricated consisting of two electrodes separated by a hydrogen silsesquioxane (HSQ) spacer. Then, the top electrode is mechanically suspended by etching the HSQ sacrificial layer, exposing the electrode surfaces for molecular layer deposition. The molecule is deposited through self-assembly, or other techniques including layer-by-layer coating and vapor phase deposition. Upon molecular layer growth, the sample undergoes controlled collapse of the top contact using capillary or electrostatic forces (Supplementary Fig. 3). Two variations of the fabrication flow are shown, where either the molecules are deposited on **(i)** both electrode surfaces, or **(ii)** only a single electrode. To limit growth to a single side, the surface of one electrode is protected with a sacrificial alumina coating which is removed post molecular layer deposition and prior to self-assembly of the contact. A chromium etch stop is leveraged to protect the alumina during the initial HSQ undercut in this version of the process. The detailed fabrication process is included in the Methods section. It should be noted that this fabrication flow offers an example and the concept can be extended to diverse other device designs, molecules, polymers and nanomaterials depending on the application of interest.

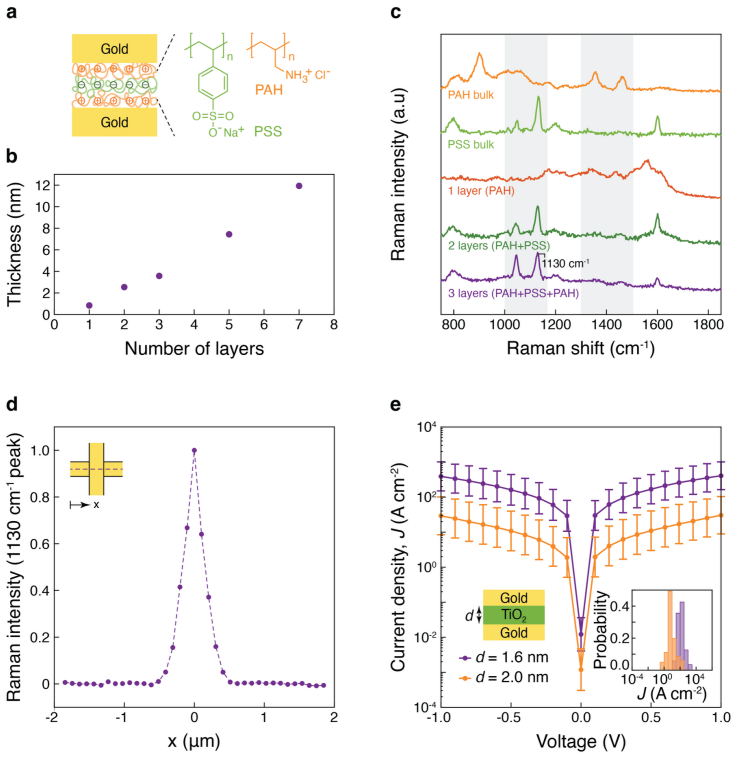

Supplementary Fig. 2 | Self-assembled contacts beyond molecular monolayers. a, Self-assembled contacts made to polymer thin films formed by layer-by-layer coating of polyelectrolytes, specifically poly(allylamine hydrochloride) (PAH) and poly(styrene sulfonate) (PSS). **b,** Ellipsometric thicknesses of polymer thin films formed from sequential coating of PAH and PSS layers. **c,** Raman spectra of devices formed with 1 to 3 layers of PAH and PSS, leading to device gap thicknesses of about 1.2 nm to 7.2 nm as the polymer deposits on both electrodes. The characteristic peaks of PSS and PAH, presented in the measurements of bulk material and highlighted in grey, are observed in the corresponding device response. **d,** Raman line scan of a three-layer device about the PSS 1130 cm^{-1} peak (integrated from 1110 cm^{-1} to 1150 cm^{-1}) showing plasmonic enhanced response at the device region, confirming successful integration. **e,** Devices fabricated with atomic layer deposited TiO_2 of two thicknesses. Here, the contacts are released through critical point drying and collapsed following vapor phase deposition of the active layer. The inset shows the distribution of current density at 0.5 V. Eighty devices per condition are measured.

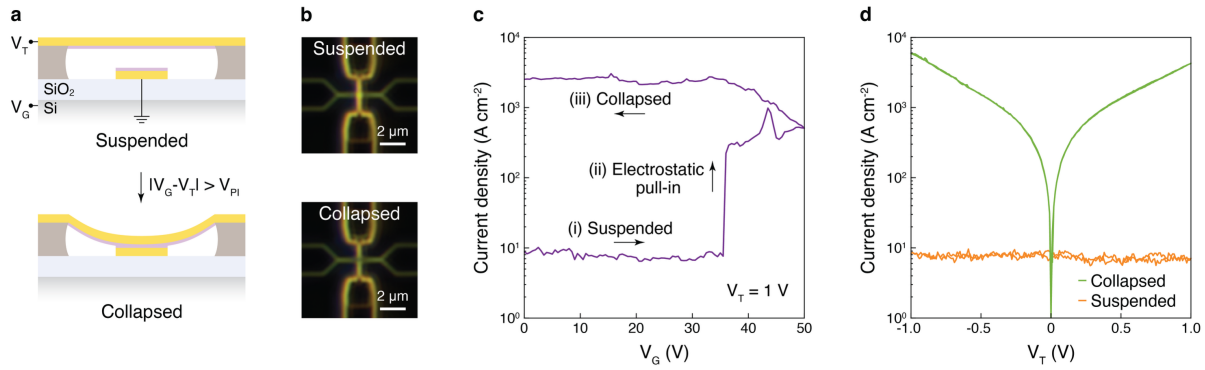

Supplementary Fig. 3 | Electrostatic contact assembly. a, Schematic illustration of the dry electrostatic contact assembly. Voltage is applied across the back-gate (V_G) and the suspended top electrode (V_T) to induce an electrostatic force that deflects the beam. When the applied voltage exceeds that needed to pull in the device (V_{PI}), the top electrode collapses and van der Waals forces hold it in contact. **b,** Darkfield optical micrographs of device before (top) and after (bottom) electrostatic collapse, where decrease in scattering in the overlap region differentiates between the initial, suspended state, and the final, collapsed state. **c,** Current measured at top electrode as gate voltage is swept from 0 V to 50 V, and back to 0 V. Beyond $V_{PI} = 36$ V, a large increase in current is observed as the beam comes into contact, and a molecular junction forms. Measured current is normalized by the expected device active area, defined as the overlap region between the top and bottom electrodes. **d,** BPT device J-V characteristic before and after electrostatic collapse. Device goes from being open, to showing tunneling characteristics consistent with devices fabricated by capillary collapse.

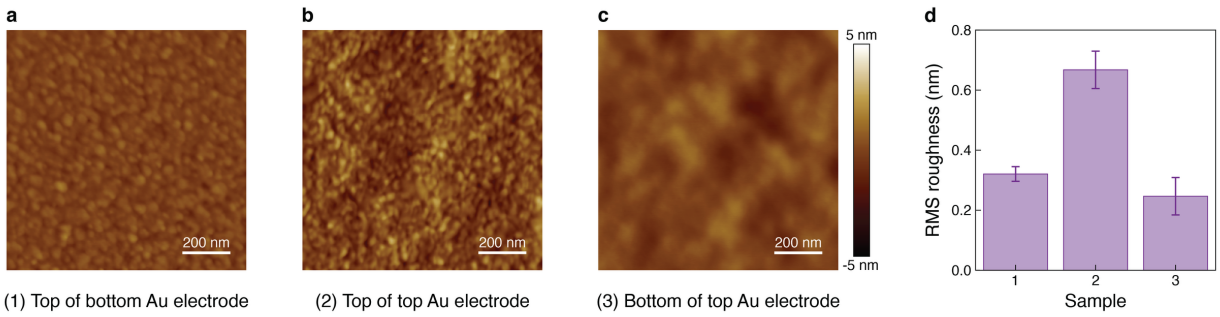

Supplementary Fig. 4 | Surface roughness of gold contacts. a-c, Atomic force microscope (AFM) surface topography map of **(a)** top surface of bottom electrode, **(b)** top surface of top electrode, and **(c)** bottom surface of top electrode. **d,** Average root-mean-square (RMS) roughness over $(200\ \text{nm})^2$ area. Error bars represent standard deviation. Surfaces in contact with the molecular layer are ultrasmooth, 0.32 nm and 0.25 nm for the bottom and top electrodes, respectively, achieved through optimized deposition and templating by the sacrificial oxide.

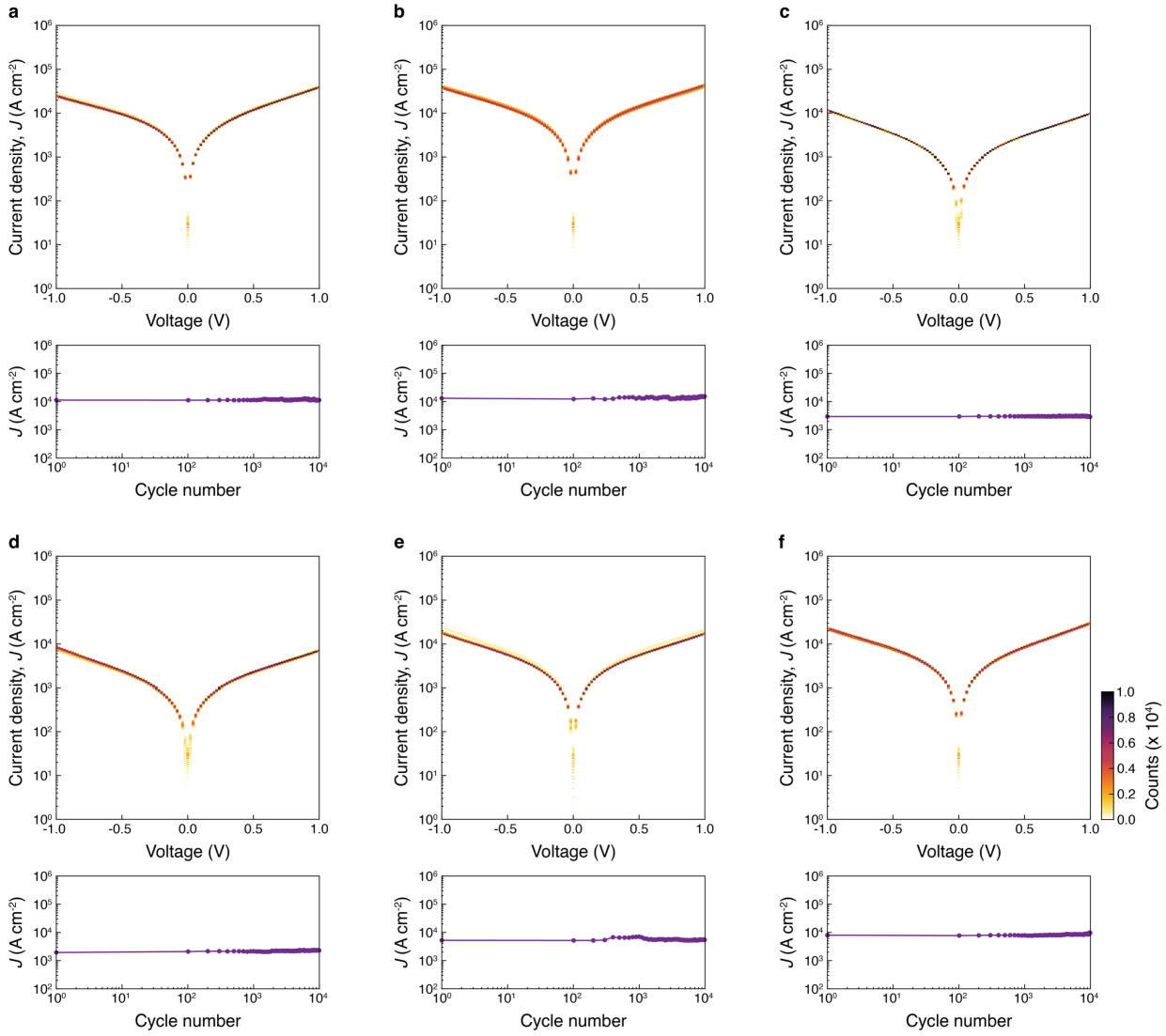

Supplementary Fig. 5 | Device endurance. a-f, J-V density plot of six BPT devices measured through 10^4 repeated cycles from 0 V to ±1 V. The bottom panels show the current density of each device at 0.5 V. All devices exhibit stable performance throughout the cycling.

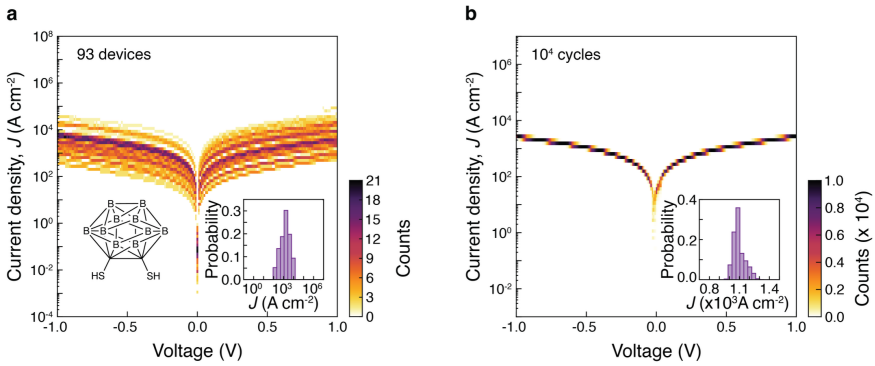

Supplementary Fig. 6 | High yield, uniformity, endurance of o-carborane-1,2-dithiol devices. **a,** J-V density plot of 93, 200 nm-wide carborane-dithiol devices fabricated with 97% yield of working devices. The insets show the structure of the molecule and the distribution of current density at 0.5 V. **b,** J-V density plot of a representative device cycled 10^4 times from 0 V to ± 1V. The inset shows the distribution of current density at 0.5 V.

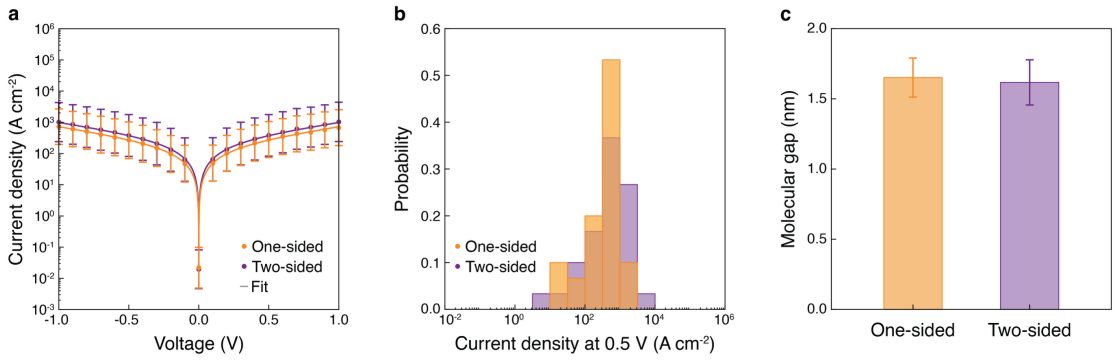

Supplementary Fig. 7 | Comparing devices with one-sided and two-sided molecular growth. **a,** J-V plot of 1,8-octanedithiol (C8) devices made using the one-sided and two-sided fabrication techniques. The mean ± standard deviation current density is plotted for 30 devices per condition. The overlaid lines are the fit to the Simmons tunneling model. **b,** Distribution of current density at 0.5 V for the devices. **c,** Molecular gap thickness of the one-sided and two-sided devices extracted by fitting the experimental results to the Simmons tunneling model, according to the process described in Supplementary Note 5. The gap thicknesses are nearly the same, 1.65 ± 0.14 nm and 1.62 ± 0.16 nm for one-sided and two-sided devices, respectively, suggesting that the two-sided devices form an interpenetrated monolayer. Despite the similarity, to ensure that the resulting SAMs are most consistent with past literature reports for effective comparison, we employed the one-sided growth technique (Methods, Supplementary Fig. 1) for testing alkanedithiols of varying lengths.

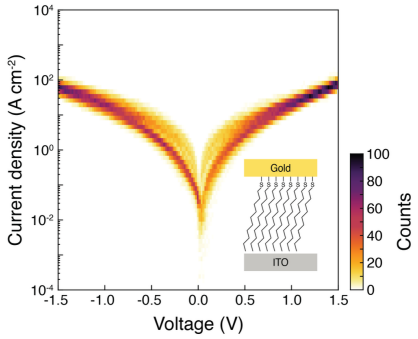

Supplementary Fig. 8 | Decanethiol control devices with an asymmetric gold-ITO junction. J-V density plot of 1-decanethiol control devices (10 devices and 10 runs per device) fabricated following the same procedure as for the viologen devices, using an ITO bottom electrode and a gold top electrode with a $AgPF_6$ treatment. These devices show no switching.

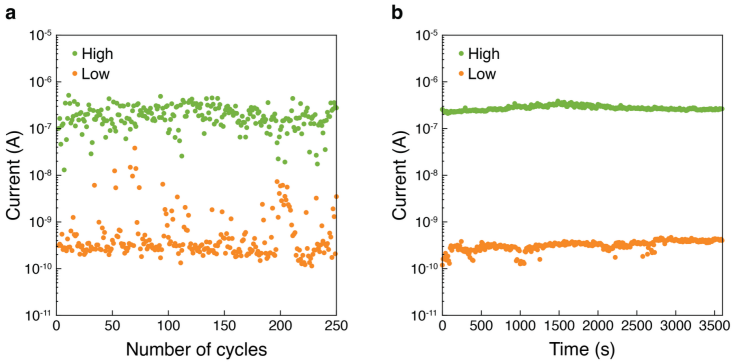

Supplementary Fig. 9 | Stability of viologen devices. a, The high and low conductance states in a viologen device with area 0.14 μm^2 over 250 repeated voltage cycles, with current measured at a read voltage of 0.5 V on positive trace and retrace. **b,** The high and low conductance state of the same device measured over time. The device is set to the high conductance state with a write voltage of 1.5 V followed by it being read at 0.5 V. A read voltage of 0.5 V was also used to probe the low conductance state.

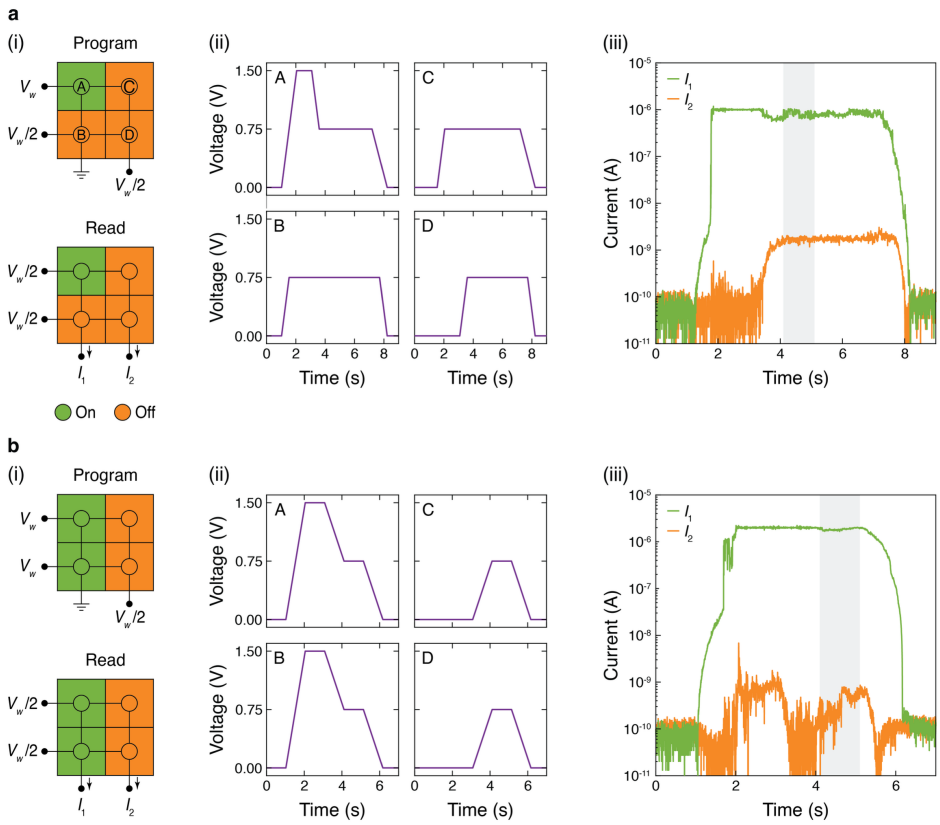

Supplementary Fig. 10 | Biasing scheme for crossbar array measurement of viologen devices. **a–b,** Biasing scheme and measurements for two programmed configurations of the 2×2 device array are presented corresponding to the results reported in Fig. 5. For each configuration, we show **(i)** schematic of the biasing during both programming and read phases, **(ii)** applied voltage across each device over time, and **(iii)** current over time at each output column. Devices are programmed based on a half-biasing scheme, where devices are selected by applying a write voltage, V_w = 1.5 V with other terminal set to 0 V, while remaining rows and columns have an applied voltage, $V_w/2$ = 0.75 V. This enables selectively writing desired devices to the high-conduction state while leaving non-selected devices in the low-conduction state. **a,** An example configuration with a single device selected and **b,** an example with two devices selected. A read voltage of $V_w/2$ = 0.75 V is used to measure the current at each column node, representing the sum of current through both devices in the column. The values reported in Fig. 5e are averaged across the grey highlighted region in (iii) during which a read voltage is applied to all devices.

SUPPLEMENTARY TABLES

Supplementary Table 1 | Benchmarking table.
A summary of major approaches reported in the literature for integrating molecular monolayers into functional devices is presented. These approaches can be broadly grouped into four categories. The first category of approaches relies on direct deposition on top of the molecular layer. Though straightforward, such approaches result in low device yields that limit integration into functional systems. Use of a protective interlayer can minimize damage during direct deposition to improve yield. However, interlayers can be incompatible with standard large-scale semiconductor processing, devices fabricated through these approaches are often limited to micron-scale dimensions, and pristine interfacing between the molecules and contact is prevented by the presence of the interlayer, influencing the performance. This non-ideal performance is evidenced by a decay coefficient (β) that differs significantly from its ideal value of 1 per carbon[1]. The use of liquid metal top contacts alleviates the shorting issues associated with direct deposition, however, the realization of stable, nanoscale contacts with wafer-scale, dense integration is challenging. Physical lamination approaches, where prefabricated top electrodes are transferred onto the molecular layer, have the potential to realize intimate contact without high rates of shorted devices. These approaches, however, are either limited by the need for adhesive anchor groups or the need for manual/wet processing on top of the molecules, limiting scalability and the ability to realize clean junctions. Our self-assembled contact approach helps simultaneously realize pristine, damage-free integration of molecular devices at nanoscale lateral dimensions and with high-yield, using standard fabrication techniques that are conducive to wafer-scale processing. Thus, it can open opportunities for integrated devices enabling practical applications.

Note: Among the parameters to be compared between various approaches is device-to-device variation. We quantify this variation through the full width at half maximum (FWHM) of the distribution of the logarithm of current density at a fixed voltage. This value is reported in Supplementary Table 1. Because conduction variations in molecular devices are typically log-normally distributed[2], this full width at half maximum is given by $\mathrm{FWHM} = 2\sqrt{2\ln 2}\,\sigma_{\log}$, where $\sigma_{\log}$ is the standard deviation of the data on a logarithmic scale. For log-normally distributed data, the distribution on a logarithmic and linear scale can further be related through $\ln(10)\,\sigma_{\log} = \sqrt{\ln(1+\sigma_{\mathrm{lin}}^2/\mu_{\mathrm{lin}}^2)}$, where σ_{lin} and μ_{lin} are the standard deviation and mean of the data taken on a linear scale[3]. To ensure consistent benchmarking, this relation is used in Supplementary Table 1 to derive $\sigma_{\log}$ from the reported σ_{lin} and μ_{lin} in works that analyze their data on a linear scale. Aside from the quality of molecular layer, the device-to-device variation is influenced by both the integration approach and the size of the device being characterized. As has previously been observed, our variation decreases with increasing feature size (Fig. 3c), with magnitude comparable to other demonstrations of nanoscale molecular devices[4–6].

Reference	Approach	Description	Yield[†]	Minimum feature size[‡]	FWHM[§]	Number of devices[¶]	Endurance[‖]	Non-standard materials/processes[††]	On-molecule processing[‡‡]	Anchor group constrained[§§]	Connection demonstrated[¶¶]	Mass-fabrication compatibility	β (per-carbon) [‖‖]
Lee et al. 2004[7]	Direct deposition	Direct deposition in nanopore	5 %	45 nm	0.1-0.3 (0.002-0.7 μm^2)[a]	–	–	None	Deposition	No	No	High	1.03 ± 0.05
Wang et al. 2007[8]	Direct deposition	Direct deposition	2 %	2 µm	0.3-1.4 (3 μm^2)[b]	10^2	–	None	Deposition	No	No	High	1.15 ± 0.1*
Akkerman et al. 2006[9]	Protective interlayer	PEDOT/PSS coating	95 %	10 µm	0.1-0.5 (70-5000 μm^2)[a]	10^1	10^2	Organic spin-coating	Spin-coating, deposition, plasma etching	Yes	No	Moderate	0.74 ± 0.06*
Neuhausen et al. 2012[4]	Protective interlayer	Aedotron coating	100 %	300 nm	0.2-0.6 (0.07-0.8 μm^2)[b]	10^1	–	Organic spin-coating	Spin-coating, deposition, plasma etching	No	No	Moderate	0.45
Preiner & Melosh 2008[10]	Protective interlayer	ALD	~100 %	50 µm	0.1-0.4 (3-5×10^4 μm^2)[a]	10^1	–	None	Deposition	Yes	No	High	0.63 ± 0.05
Puebla-Hellmann et al. 2018[5]	Protective interlayer	Nanoparticle interlayer	100 %	60 nm	0.3-2.6 (0.003-4000 μm^2)[c]	10^3	–	Nanoparticle spin-coating	Spin-coating, deposition	Yes	No	High	1.0 ± 0.2*
Seo et al. 2012[11]	Protective interlayer	rGO interlayer	>99 %	100 µm	0.2-0.3 (1×10^4 μm^2)[a]	10^2	10^2	rGO spin-coating	Deposition	No	No	Low	1.01 ± 0.15
Wang et al. 2011[12]	Protective interlayer	Graphene interlayer	98.1 %	4 µm	0.3-0.7 (10 μm^2)[a]	10^2	10^3	Graphene transfer	Deposition, plasma etching	No	No	Low	1.06 ± 0.14
Cao et al. 2024[6]	Liquid metal	EGaIn printing	90 %	500 nm	0.8-1.1 (0.2-1000 μm^2)[b]	10^3	10^4	EGaIn stamping	None	No	Yes	Moderate	1.09
Wan et al. 2014[13]	Liquid metal	EGaIn microfluidics	88 %	35 µm	0.3-0.6 (1000 μm^2)[b]	10^3	10^3	EGaIn microfluidics	None	No	No	Low	1.0 ± 0.03
Bof Bufon et al. 2011[14]	Physical lamination	Strained nanomembrane	90 %	Ill-defined	0.3 (< 1 μm^2)[a]	10^1	–	None	Wet etching	No	No	Moderate	1.01 ± 0.05
Jeong et al. 2016[15]	Physical lamination	Direct transfer	70 %	2 µm	0.8-2.4 (10-80 μm^2)[b]	10^2	–	PMMA-mediated transfer	Wet etching	No	No	Low	1.32 ± 0.04
Krabbenborg et al. 2013[16]	Physical lamination	Wet transfer	50 %	10 µm	1.4-2.7 (100-400 μm^2)[b]	10^1	10^1	Wet transfer	Wet lamination	No	No	Low	0.73 ± 0.06
Niskala et al. 2012[17]	Physical lamination	Transfer printing	96 %	80 nm	0.2-0.5 (0.005-50 μm^2)[a]	10^2	–	Transfer printing	None	Yes	No	Low	0.98 ± 0.11*
This work	Self-assembled contacts	Stiction assembly	99 %	100 nm	0.5-1.7 (0.01-0.4 μm^2)[d]	10^3	10^5	None	None	No	Yes	High	1.01 ± 0.08*

[†] Maximum value reported. [‡] Minimum lateral dimensions reported.

[§] Full width at half maximum (FWHM) of distribution on a logarithmic scale, as described in the note. Reported sizes represent range over which variation is characterized.

[¶] Maximum number of devices reported for a single type of molecule.

[‖] Maximum cycles reported for a single device. – Indicates no direct discussion of endurance.

[††] Employed materials/processes that are non-typical to wafer-scale semiconductor processing.

[‡‡] Processing beyond rinsing/physical contacting that is performed on top of molecular layer.

[§§] Whether a specific top-anchor group (e.g. thiol) is required for successful device fabrication.

[¶¶] Whether work reports application involving multiple devices integrated on chip.

[‖‖] Reported decay coefficient, based on measurement of current density as a function of alkyl molecule length. *Indicates results for alkanedithiols.

[a] Variation reported on a linear scale, converted to logarithmic variation as described in the table caption. [b] Variation reported on a logarithmic scale. [c] Variation extracted from source data. [d] Variation based on data in Fig. 3c.

SUPPLEMENTARY NOTES

Supplementary Note 1 | Collapse characterization

We used darkfield optical microscopy to characterize whether a device is collapsed or suspended, where a decrease in darkfield scattering corresponds to the collapsed state. We validated this approach by confirming whether devices are collapsed or suspended through SEM imaging. Darkfield and SEM images of example 350 nm-wide BPT molecular junctions are shown in Supplementary Fig. 11a. Compared to SEM, darkfield microscopy allows for rapid classification of collapsed and suspended features without damaging the molecules due to exposure to a high energy electron beam. An example classified array of structures is shown in Supplementary Fig. 11b-c. These device dimensions were specifically chosen to provide examples of both suspended and collapsed structures, whereas the device dimensions used in the rest of the work are optimized for near 100% collapse yield.

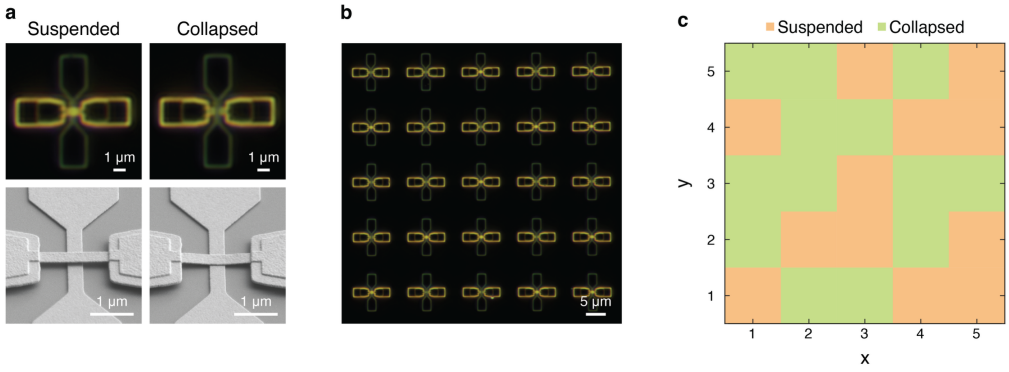

Supplementary Fig. 11 | Classifying successful collapse. a, Two devices imaged using darkfield microscopy (top) and SEM (bottom), demonstrating that reduced scattering at the center of the crossbar in the darkfield image corresponds to the collapsed state. **b,** An array of devices imaged under darkfield and **c,** their corresponding classification.

Supplementary Note 2 | Modeling of the contact self-assembly

Successful self-assembly of contacts requires two conditions to be met. First, the applied assembly forces must overcome the elastic restoring force of the suspended structure. Second, the adhesive forces must be sufficient to hold the structure in this state.

In our demonstrated approach, capillary forces (F_c) enable the collapse during drying. For a doubly clamped beam, assuming no residual stress, the ratio of capillary forces to elastic restoring forces is given by the elastocapillary number, N_{ec}:[18,19]

$$N_{ec} = \frac{128 E g_{s_0}^2 t^3}{15 \gamma_l \cos\theta_c \, l^4 (1 + t/w)} \quad (1)$$

where E, t, w, l are the Young's modulus, thickness, width and length of the beam respectively, g_{s_0} is the as-fabricated gap between the top electrode and the substrate, γ_l is the surface tension of the liquid, and θ_c is the contact angle of the liquid. We conduct collapse with ethanol, which is fully wetting on our chips ($\theta_c = 0°$) and has a surface tension of $21.91\ \mathrm{mN/m}$[20]. The green dashed line in Fig. 1f represents the boundary where capillary forces are equal to elastic restoring forces. To the right of this line, capillary forces dominate over elastic restoring forces ($N_{ec} < 1$), enabling reliable capillary collapse.

In the collapsed state, the balance of adhesive forces with elastic restoring forces can be analyzed using the method in [21]. The total energy of the system is given by:

$$U = U_e + U_a = \frac{128 E g_0^2 t^3 w}{15(l - l_c)^3} + 2\gamma_s l_c w \tag{2}$$

where U_e and U_a are the elastic and adhesive energies, respectively, g_0 is the as-fabricated gap between the top and bottom electrodes, l_c is the contact length between these electrodes in the collapsed state, and γ_s is the surface energy of the electrodes. For BPT-coated gold, $\gamma_s = 86.8\ \mathrm{mN/m}$ [22]. Differentiating this energy with respect to l_c gives the elastic ($F_e = \partial U_e / \partial l_c$) and adhesive ($F_a = \partial U_a / \partial l_c$) forces that account for contact delamination and stiction, respectively. Their ratio is given by:

$$\frac{F_e}{F_a} = \frac{64 E g_0^2 t^3}{5\gamma_s (l - l_c)^4} \tag{3}$$

The orange dashed line in Fig. 1f represents the boundary where (3) is equal to 1 and l_c is equal to the width of the bottom beam. To the right of this line, the restoring forces are insufficient to delaminate a structure once it is collapsed, and hence, stiction dominates.

For our tested geometries in Fig. 1, this analysis predicts that the limiting step to contact formation is the capillary collapse, since devices that collapse are all beyond the stiction threshold. This is consistent with our experimental results, where high-yield collapse is achieved to the right of the elastocapillary boundary.

Supplementary Note 3 | Characterization of the BPT and alkanedithiol molecular layers

X-ray photoelectron spectroscopy (XPS) characterization

To confirm successful molecular assembly, we acquired S 2p XPS spectra of the alkanedithiol and BPT monolayers, shown in Supplementary Fig. 12. We fit the S 2p spectra using 2p doublets with a 2:1 peak area ratio for S $2p_{3/2}$ and S $2p_{1/2}$, respectively, having a 1.18 eV splitting. For the alkanedithiols, two distinct S 2p environments are observed, including the chemisorbed surface-bound species (S $2p_{3/2}$ binding energy (BE) ~161.9 eV; orange trace) and the unbound thiol (S $2p_{3/2}$ BE ~163.4 eV; green trace)[23]. We observed one S 2p state for BPT, corresponding to its chemisorbed thiol species (S $2p_{3/2}$ BE ~162.0 eV) without additional physiosorbed components. No oxidized sulfur species (BE > 166 eV)[24] were observed in any case, indicating well-formed monolayers. The samples were prepared on gold substrates template-stripped off of HSQ, resembling the surface of the top electrode in the device.

Electrochemical characterization

Reductive desorption measurements of the alkanedithiol and BPT self-assembled monolayers were taken in 0.5 M KOH (aq) (> 99.99%, MilliporeSigma) at scan rates between 50 mV s^{-1} and 125 mV s^{-1} to determine their surface coverage. The electrochemical cell consisted of an Ag/AgCl (1 M KCl) reference electrode (CH Instruments CHI111), a Pt wire counter electrode (CH Instruments CHI115), and a template-stripped gold working electrode functionalized with the monolayers. We calculated the surface coverage $\Gamma = Q/nFA$ (mol/cm^2), where Q is the integrated charge (C) corresponding to the desorption process, n corresponds to the moles of electron per reaction (= 1 mol), F is Faraday's constant (= 96485 C/mol), and A is the electrode area. The responses corresponding to thiol desorption from multiple gold lattice environments were integrated to give Q[25,26]. We determined the electrochemical surface area (ECSA), A = 0.83 cm^2, by acquiring voltammograms of freshly template-stripped gold in N_2-purged 0.5 M H_2SO_4 (aq) at 50 mV s^{-1} from 0 to +1.5 V vs. Ag/AgCl and integrating the reduction peak of gold oxide, assuming a 390 µC cm^{-2} charge density for a monolayer of oxygen chemisorbed on the electrode[27]. The measured coverages, given in Supplementary Table 2, agree with the theoretical value of Γ = 7.6 × 10^{-10} mol cm^{-2} for ideal packing on an Au(111) lattice, suggesting densely formed monolayers.

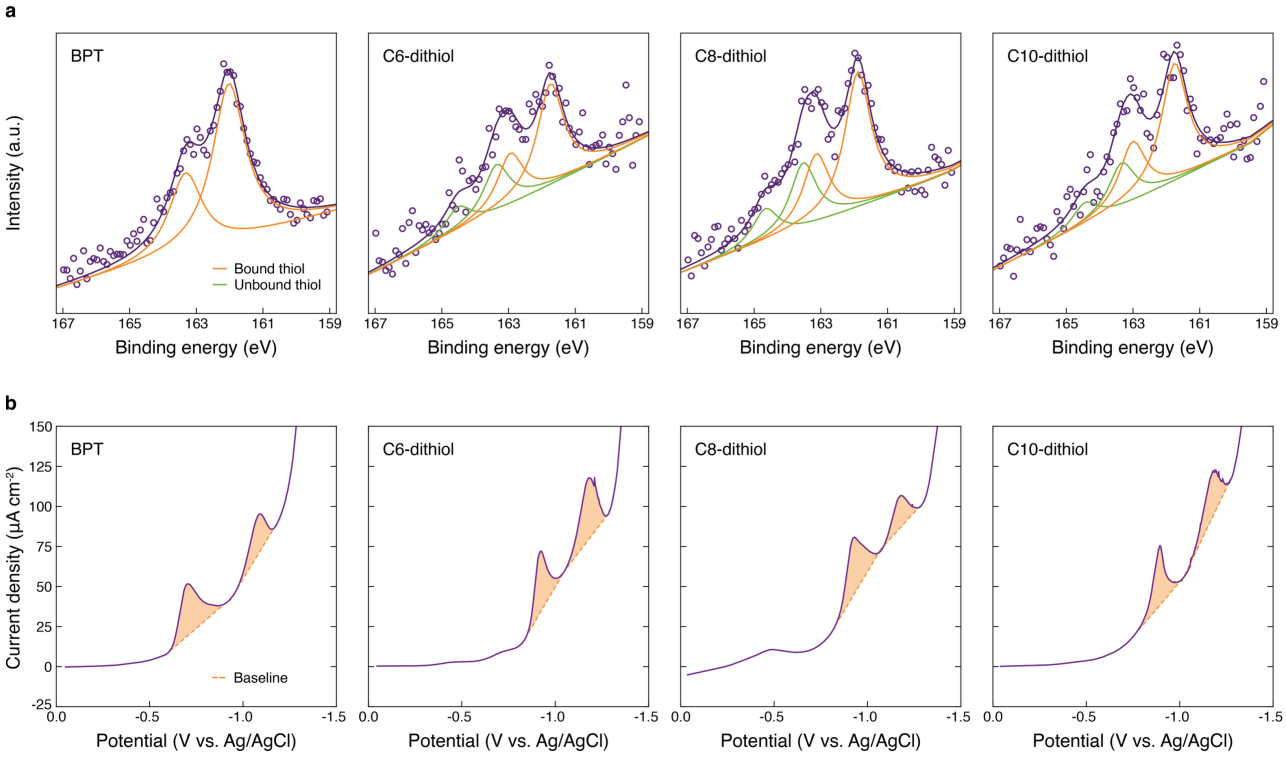

Supplementary Fig. 12 | Characterization of self-assembled monolayers. a, S 2p XPS spectra of BPT, C6-dithiol, C8-dithiol, and C10-dithiol on gold substrate. The spectral fits denoted by orange traces (S $2p_{3/2}$ BE ~ 162 eV) correspond to the chemisorbed surface-bound thiol, while the green traces (S $2p_{3/2}$ BE ~ 163.4 eV) present in the alkanedithiol samples are assigned to the unbound thiol species. **b,** Reductive desorption voltammograms of BPT, C6-dithiol, C8-dithiol, and C10-dithiol monolayers on gold substrate taken at 75 mV s^{-1} showing the linear baselines (dashed line) and the peak area of the two major regions (shaded in orange).

Supplementary Table 2 | Measured surface coverage. BPT and alkanedithiol surface coverage values evaluated from the reductive desorption measurements.

Monolayer	Coverage (mol cm^{-2})
BPT	$7.47 \pm 1.65 \times 10^{-10}$
C6-dithiol	$6.62 \pm 0.80 \times 10^{-10}$
C8-dithiol	$8.10 \pm 0.98 \times 10^{-10}$
C10-dithiol	$7.40 \pm 0.56 \times 10^{-10}$

Supplementary Note 4 | Classification of the device performance

We classified the devices as shorted, open, or working based on their measured current from -1 V to +1 V. During measurement, the current compliance limit was set to 1 mA. If the measured current reached the compliance limit, the device was classified as shorted. If at no point the current exceeded 100 pA, the device was classified as open. Otherwise, the device was classified as working. Supplementary Fig. 13 shows example devices drawn from the data used in Fig. 3.

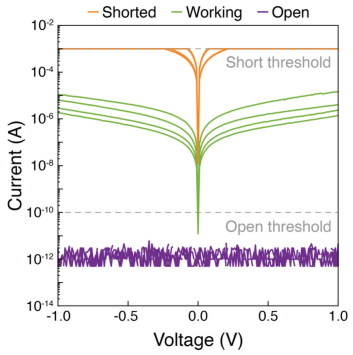

Supplementary Fig. 13 | Performance classification. Example current-voltage characteristics for devices classified as shorted, working and open. Dashed lines are thresholds for short and open.

Supplementary Note 5 | Simmons fitting

Measured tunneling current (I) as a function of applied voltage (V) is fitted to the Simmons tunneling model[28], which has been shown to accurately describe non-resonant tunneling through alkanethiol junctions[29–31,17]. In this model, current through the molecular layer is given by:

$$I = \left(\frac{qA}{4\pi^2\hbar g^2}\right)\left[\left(\phi - \frac{qV}{2}\right)\exp\left(-\frac{2g\alpha\sqrt{2m_e(\phi - qV/2)}}{\hbar}\right) - \left(\phi + \frac{qV}{2}\right)\exp\left(-\frac{2g\alpha\sqrt{2m_e(\phi + qV/2)}}{\hbar}\right)\right] \quad (4)$$

where m_e and q are the mass and charge of an electron, $\hbar$ is the reduced Plank's constant and A is the junction area. The fitting parameters are g, the tunneling gap, ϕ, the tunneling barrier, and

α, the non-ideality factor. The Simmons model was fitted to the experimental data using non-linear least-squares minimization, with the Trust-Region algorithm in MATLAB. Because g, ϕ and α are strongly correlated, the fitted values are sensitive to the initial values which are chosen for these parameters. To minimize the effect of these correlations, fitting was repeatedly performed with the fit parameters initialized to values randomly sampled from a valid range. g, ϕ and α were constrained to lie within 1–2.5 nm, 1–3 eV and 0.5–0.7, respectively, spanning the range of these values reported in the literature[17,29,30,32,33]. Each device was fitted 1000 times using different starting points. We expect that different devices fabricated with the same molecule should share ϕ and α, with variations in the tunneling gap stemming from device-to-device variations. Thus, after fitting g, ϕ and α to all devices, the measurements were re-fitted, fixing ϕ and α to their average values for each molecule, with g being the only per-device fit parameter.

For C8-dithiol, the best fit values for ϕ and α were 2.25 ± 0.26 eV and 0.59 ± 0.06, respectively (mean ± standard deviation). Assuming these values, the chips fabricated using the two-sided and one-sided approaches had an average gap of 1.62 ± 0.16 nm and 1.65 ± 0.14 nm, respectively. C6-dithiol had g, ϕ, and α of 1.47 ± 0.09 nm, 2.12 ± 0.20 eV and 0.57 ± 0.05, respectively. C10-dithiol had g, ϕ and α of 1.73 ± 0.16 nm, 2.16 ± 0.46 eV and 0.64 ± 0.08, respectively. The lines shown in Fig. 4a and Supplementary Fig. 7 represent the fit based on average values of ϕ and α.

Supplementary Note 6 | Viologen molecule synthesis and characterization

Materials

All deuterated solvents were purchased from Cambridge Isotope Laboratories. Iodomethane, acetyl chloride, tetrabutylammonium chloride, NH_4PF_6, dry methanol, dichloromethane, acetone and acetonitrile were purchased from MilliporeSigma. 4,4-bipyridine and 11-bromo-1-undecyl thioacetate were purchased from Ambeed. All reactions were performed in flame-dried glassware under inert atmosphere unless otherwise stated.

Solution-state nuclear magnetic resonance (NMR) spectroscopy

^{1}H NMR spectra were collected at room temperature (25 °C) using either a three-channel Bruker Avance NEO 500 MHz spectrometer or a two-channel Bruker Avance-III HD NanoBay 400 MHz spectrometer. Data was analyzed with MestReNova version 14.1.0-24037. Chemical shifts are expressed in parts per million (ppm), and splitting patterns are designated as s (singlet), d (doublet), t (triplet), q (quartet), m (multiplet), and b (broad). Scalar coupling constants (*J*) are reported in Hertz (Hz).

Synthesis

The viologen molecule (compound **4**) was synthesized using the procedure in [34], and illustrated in Supplementary Fig. 14. The different steps of the synthesis are described below.

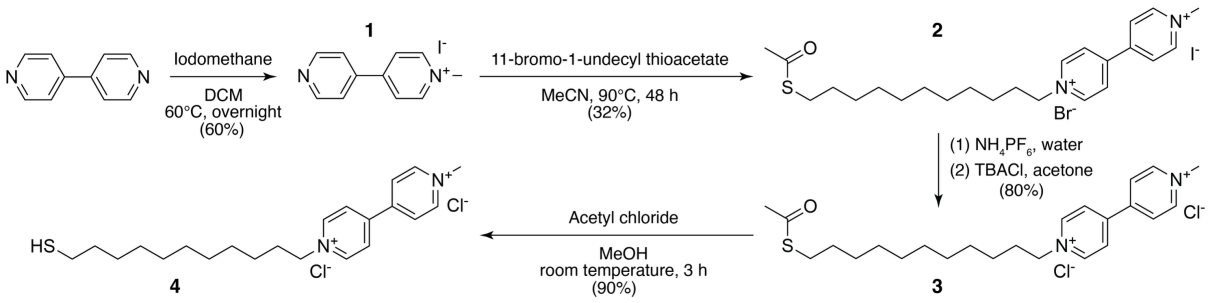

Supplementary Fig. 14 | Viologen molecule synthesis scheme. Steps **1**–**4** are described below.

Synthesis of compound 1. In a round bottom flask, 4,4-bipyridine (10 g, 64 mmol, 1 eq.) was dissolved in 30 mL of dichloromethane (DCM). A solution of iodomethane (5 mL, 81.2 mmol, 1.27 eq.) in DCM (150 mL) was then added dropwise over 30 min. The reaction mixture was refluxed overnight at 60 °C. All volatiles were removed under reduced pressure, and the resulting solid was washed with toluene to remove the unreacted starting materials. The solid was then dissolved in acetonitrile, filtered and concentrated to yield compound **1** (11.44 g, 60%). The resulting material shows characteristic ^{1}H NMR (Supplementary Fig. 15a) consistent with literature[34]. ^{1}H NMR (500 MHz, Methanol-d$_4$): δ 9.08 – 9.03 (m, 2H), 8.88 – 8.82 (m, 2H), 8.59 – 8.46 (m, 2H), 8.08 – 7.94 (m, 2H), 4.49 (s, 3H).

Synthesis of compound 2. In a round bottom flask, compound **1** (1.3 g, 4.36 mmol, 1 eq.) and 11-bromo-1-undecyl thioacetate (2.0 g, 6.47 mmol, 1.5 eq) were dissolved in acetonitrile (130 mL). The mixture was refluxed for 48 hours at 90 °C before being concentrated at reduced pressure. The resulting solid was washed with toluene (5× 50 mL) followed by acetonitrile (2× 20 mL). The resulting orange solid was then dried, yielding pure compound **2** (0.87 g, 32%). The resulting material shows characteristic ^{1}H NMR (Supplementary Fig. 15b) consistent with literature[34]. ^{1}H NMR (400 MHz, Methanol-d$_4$): δ 9.32 – 9.26 (m, 2H), 9.23 – 9.17 (m, 2H), 8.68 (t, J = 6.5 Hz, 4H), 4.76 (t, J = 7.6 Hz, 2H), 4.54 (s, 3H), 2.85 (t, J = 7.3 Hz, 2H), 2.30 (s, 3H), 2.10 (p, J = 7.6 Hz, 2H), 1.60 – 1.24 (m, 18H).

Synthesis of compound 3. To a solution of compound **2** (870 mg, 1.42 mmol) in water (100 mL), 52 mL of 1 M NH_4PF_6 aqueous solution was added. The resulting precipitate was filtered and washed with water (3× 30 mL) and dried under vacuum. The white precipitate was dissolved in acetone (35 mL). Subsequently, 52 mL of 1 M solution of tetrabutylammonium chloride (TBACl) in acetone was added, causing precipitation of the desired chloride salt. The solid was filtered, washed with acetone (3× 30 mL) and dried under vacuum, yielding compound **3** (550 mg, 80%).

Synthesis of compound 4. To a solution of compound **3** (550 mg, 1.1 mmol) in dry methanol (110 mL), acetyl chloride (16 mL) was added slowly at -78 °C. After 15 min, the solution was allowed to heat up to room temperature and stirred for 3 hours. The mixture was concentrated under reduced pressure and washed with acetonitrile (3× 10 mL) and dried under reduced pressure to yield the viologen molecule (compound **4**) (450 mg, 90%) as a colorless solid. The material shows characteristic ^{1}H NMR (Supplementary Fig. 15c) consistent with literature[34]. ^{1}H NMR (400 MHz, Methanol-d$_4$): δ 9.31 (d, J = 6.1 Hz, 2H), 9.21 (d, J = 6.1 Hz, 2H), 8.70 (t, J = 7.0 Hz,

4H), 4.77 (t, *J* = 7.5 Hz, 2H), 4.56 (s, 3H), 2.50 (tt, *J* = 7.0, 1.1 Hz, 2H), 2.12 (t, *J* = 7.3 Hz, 2H), 1.60 (p, *J* = 7.2 Hz, 2H), 1.55 – 1.27 (m, 16H).

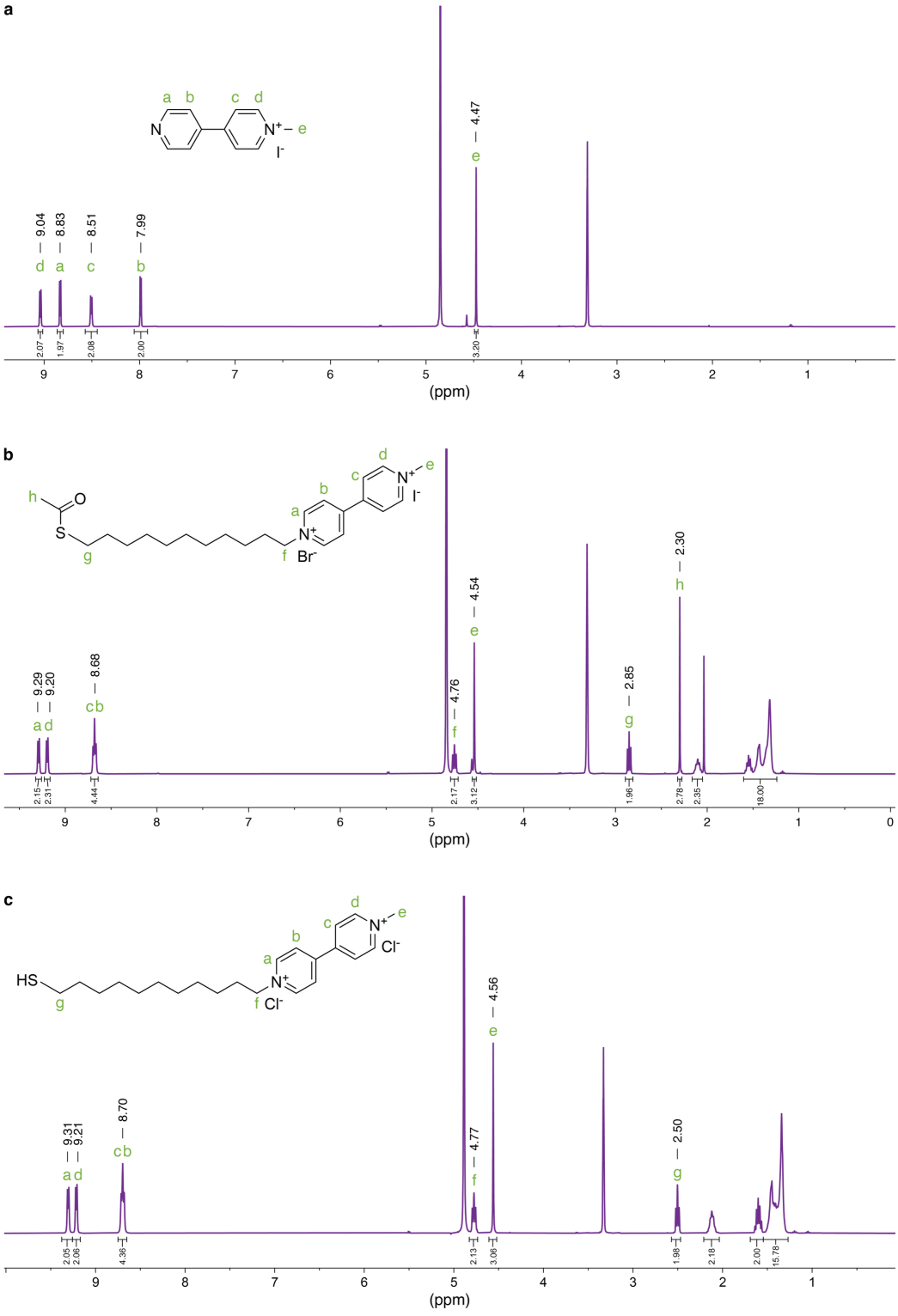

Supplementary Fig. 15 | ^{1}H NMR spectra in Methanol-d$_4$. The ^{1}H NMR spectra for **a,** compound **1**, **b,** compound **2** and **c,** compound **4**.

X-ray photoelectron spectroscopy (XPS) characterization

Once synthesized, the viologen molecules (compound **4**) were incorporated into the devices as a self-assembled monolayer formed on the gold electrode along with a $AgPF_6$ treatment. To confirm successful growth of the viologen monolayers, we performed XPS. The results are shown in Supplementary Fig. 16. The S 2p spectrum agrees with previously reported spectra of viologen SAMs and is dominated by chemisorbed thiol at a binding energy (BE) of ~ 162 eV[34,35]. The C 1s spectrum shows peak splitting consistent with C-C/C=C (~ 285.0 eV) and C-N^+ (~ 286.6 eV) environments corresponding to the viologen unit. Furthermore, the N 1s spectrum shows two environments that are attributed to $N^{\bullet}$ formed from X-ray excitation in the instrument chamber (~ 400.0 eV) and the N^+ present in the viologen units (~ 402.5 eV)[36]. We also observe a Cl 2p signal corresponding to the chloride counterion (Cl $2p_{3/2}$ BE ~ 197.4 eV). The $AgPF_6$ treatment was confirmed by F 1s (~ 686.8 eV) and Ag 3d (Ag $3d_{5/2}$ BE ~ 367.9 eV) signals present.

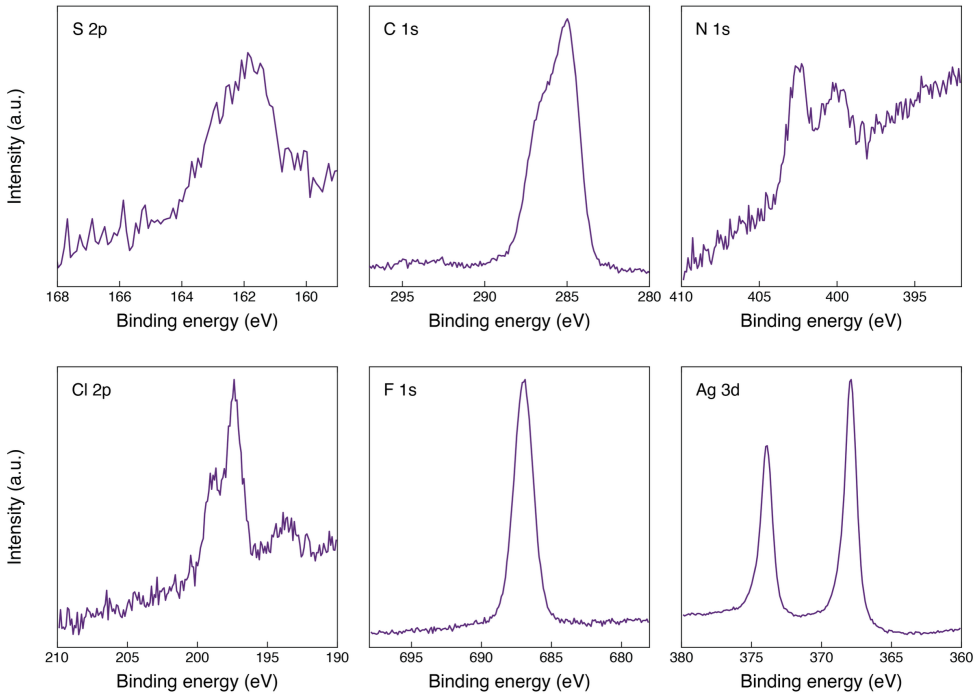

Supplementary Fig. 16 | XPS of viologen monolayers. S 2p, C 1s, N 1s, Cl 2p, F 1s and Ag 3d XPS spectra of the $AgPF_6$-treated monolayer of viologen molecules (compound **4**) on template-stripped gold.

Electrochemical characterization

To confirm the quality of the viologen monolayers, we used cyclic voltammetry with a custom-built electrochemical cell. The system consisted of a Ag/AgCl (1 M KCl) reference electrode (CH Instruments CHI111), a Pt wire counter electrode (CH Instruments CHI115), and a template-stripped gold working electrode functionalized with the viologen molecule ($SH(CH_2)_{11}MV^{2+}$) monolayer. Cyclic voltammograms (CVs) were recorded with a CH Instruments CHI660D potentiostat at a scan rate of 200 mV s^{-1} using 0.1 M NaCl (aq.) (> 99.5%, Sigma-Aldrich)

electrolyte, shown in Supplementary Fig. 17. We observed the characteristic successive redox waves corresponding to methylviologen (MV) charge states $MV^{2+} \rightleftarrows MV^{\bullet+}$ (~ −0.4 V vs. Ag/AgCl) and $MV^{\bullet+} \rightleftarrows MV^{0}$ (~ −0.8 V vs. Ag/AgCl). The first redox wave shows two characteristic components associated with the reduction of MV^{2+} to $MV^{\bullet+}$ (E_{FWHM} = 142 mV, orange trace) and dimerization of $MV^{\bullet+}$ units to form $[MV^{\bullet+}]_2$ (E_{FWHM} = 94 mV, green trace), which suggests that our monolayers are well-formed and have sufficient surface coverage to facilitate dimerization[34,37]. We determined the surface coverage $\Gamma = Q/nFA$ where Q is the charge accumulated from integrating the redox wave, n is the number of electrons per mole of reaction, and F is Faraday's constant. We found $\Gamma = 4.86 \pm 0.38 \times 10^{-10}$ mol cm^{-2}, which agrees with the coverages reported in [34] and [37].

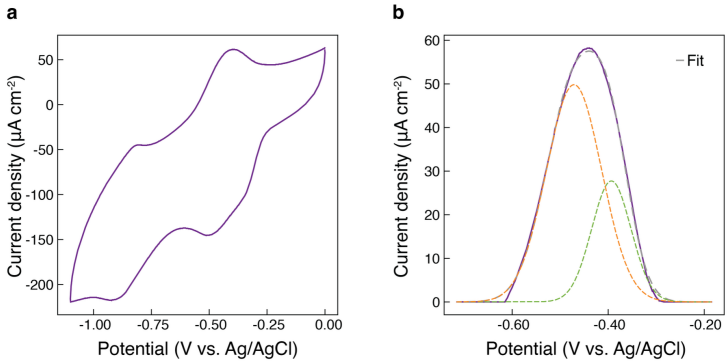

Supplementary Fig. 17 | Viologen cyclic voltammetry. a, Cyclic voltammogram of the viologen molecule ($SH(CH_2)_{11}MV^{2+}$) monolayer taken in 0.1 M NaCl at 200 mV s^{-1}. **b**, The corresponding deconvolution of the first anodic wave of the voltammogram showing contributions from $[MV^{\bullet+}]_2$ formation (green trace) and reduction of MV^{2+} to $MV^{\bullet+}$ (orange trace).

SUPPLEMENTARY REFERENCES

1. Akkerman, H. B. & de Boer, B. Electrical conduction through single molecules and self-assembled monolayers. *J. Phys. Condens. Matter* **20**, 013001 (2007).
2. Reus, W. F. *et al.* Statistical tools for analyzing measurements of charge transport. *J. Phys. Chem. C* **116**, 6714–6733 (2012).
3. Forbes, C., Evans, M., Hastings, N. & Peacock, B. *Statistical Distributions*. (John Wiley & Sons, Ltd, 2010). doi:10.1002/9780470627242.
4. Neuhausen, A. B., Hosseini, A., Sulpizio, J. A., Chidsey, C. E. D. & Goldhaber-Gordon, D. Molecular junctions of self-assembled monolayers with conducting polymer contacts. *ACS Nano* **6**, 9920–9931 (2012).
5. Puebla-Hellmann, G., Venkatesan, K., Mayor, M. & Lörtscher, E. Metallic nanoparticle contacts for high-yield, ambient-stable molecular-monolayer devices. *Nature* **559**, 232–235 (2018).
6. Cao, Z. *et al.* Flexible crossbar molecular devices with patterned EGaIn top electrodes for integrated all-molecule-circuit implementation. *Adv. Mater.* **36**, 2406456 (2024).
7. Lee, T. *et al.* Comparison of electronic transport characterization methods for alkanethiol self-assembled monolayers. *J. Phys. Chem. B* **108**, 8742–8750 (2004).
8. Wang, G., Kim, T.-W., Lee, H. & Lee, T. Influence of metal-molecule contacts on decay coefficients and specific contact resistances in molecular junctions. *Phys. Rev. B* **76**, 205320 (2007).
9. Akkerman, H. B., Blom, P. W. M., de Leeuw, D. M. & de Boer, B. Towards molecular electronics with large-area molecular junctions. *Nature* **441**, 69–72 (2006).
10. Preiner, M. J. & Melosh, N. A. Creating large area molecular electronic junctions using atomic layer deposition. *Appl. Phys. Lett.* **92**, 213301 (2008).
11. Seo, S. *et al.* Solution-processed reduced graphene oxide films as electronic contacts for molecular monolayer junctions. *Angew. Chem. Int. Ed.* **51**, 108–112 (2012).
12. Wang, G., Kim, Y., Choe, M., Kim, T.-W. & Lee, T. A new approach for molecular electronic junctions with a multilayer graphene electrode. *Adv. Mater.* **23**, 755–760 (2011).
13. Wan, A., Jiang, L., Sangeeth, C. S. S. & Nijhuis, C. A. Reversible soft top-contacts to yield molecular junctions with precise and reproducible electrical characteristics. *Adv. Funct. Mater.* **24**, 4442–4456 (2014).
14. Bof Bufon, C. C. *et al.* Hybrid organic/inorganic molecular heterojunctions based on strained nanomembranes. *Nano Lett.* **11**, 3727–3733 (2011).
15. Jeong, H. *et al.* Statistical investigation of the length-dependent deviations in the electrical characteristics of molecular electronic junctions fabricated using the direct metal transfer method. *J. Phys. Condens. Matter* **28**, 094003 (2016).
16. Krabbenborg, S. O., Wilbers, J. G. E., Huskens, J. & van der Wiel, W. G. Symmetric large-area metal-molecular monolayer-metal junctions by wedging transfer. *Adv. Funct. Mater.* **23**, 770–776 (2013).
17. Niskala, J. R. *et al.* Tunneling characteristics of Au–alkanedithiol–Au junctions formed via nanotransfer printing (nTP). *J. Am. Chem. Soc.* **134**, 12072–12082 (2012).
18. Mastrangelo, C. H. & Hsu, C. H. Mechanical stability and adhesion of microstructures under capillary forces. I. Basic theory. *J. Microelectromechanical Syst.* **2**, 33–43 (1993).
19. Bassett, D. W. Capillary pattern collapse: Prediction and prevention from past to future. *ECS Trans.* **92**, 95 (2019).
20. Haynes, W. M. *CRC Handbook of Chemistry and Physics*. (CRC Press, 2015).

21. Mastrangelo, C. H. & Hsu, C. H. Mechanical stability and adhesion of microstructures under capillary forces. II. Experiments. *J. Microelectromechanical Syst.* **2**, 44–55 (1993).
22. Bhushan, B. & Liu, H. Nanotribological properties and mechanisms of alkylthiol and biphenyl thiol self-assembled monolayers studied by AFM. *Phys. Rev. B* **63**, 245412 (2001).
23. Millone, M. A. D. *et al.* Self-assembly of alkanedithiols on Au(111) from solution: Effect of chain length and self-assembly conditions. *Langmuir* **25**, 12945–12953 (2009).
24. Castner, D. G., Hinds, K. & Grainger, D. W. X-ray photoelectron spectroscopy sulfur 2p study of organic thiol and disulfide binding interactions with gold surfaces. *Langmuir* **12**, 5083–5086 (1996).
25. Ramos, N. C., Medlin, J. W. & Holewinski, A. Electrochemical stability of thiolate self-assembled monolayers on Au, Pt, and Cu. *ACS Appl. Mater. Interfaces* acsami.3c01224 (2023).
26. Doneux, Th., Steichen, M., De Rache, A. & Buess-Herman, Cl. Influence of the crystallographic orientation on the reductive desorption of self-assembled monolayers on gold electrodes. *J. Electroanal. Chem.* **649**, 164–170 (2010).
27. Feng, G. *et al.* Studies on the effect of electrode pretreatment on the coverage of self-assembled monolayers of dodecanethiol on gold by electrochemical reductive desorption determination. *Analyst* **136**, 5058–5063 (2011).
28. Simmons, J. G. Generalized formula for the electric tunnel effect between similar electrodes separated by a thin insulating film. *J. Appl. Phys.* **34**, 1793–1803 (1963).
29. Wang, W., Lee, T. & Reed, M. A. Mechanism of electron conduction in self-assembled alkanethiol monolayer devices. *Phys. Rev. B* **68**, 035416 (2003).
30. Wang, W., Lee, T. & Reed, M. A. Elastic and inelastic electron tunneling in alkane self-assembled monolayers. *J. Phys. Chem. B* **108**, 18398–18407 (2004).
31. Vilan, A. Analyzing molecular current-voltage characteristics with the Simmons tunneling model: scaling and linearization. *J. Phys. Chem. C* **111**, 4431–4444 (2007).
32. Engelkes, V. B., Beebe, J. M. & Frisbie, C. D. Length-dependent transport in molecular junctions based on SAMs of alkanethiols and alkanedithiols: Effect of metal work function and applied bias on tunneling efficiency and contact resistance. *J. Am. Chem. Soc.* **126**, 14287–14296 (2004).
33. Majumdar, N. *et al.* Nanowell device for the electrical characterization of metal–molecule–metal junctions. *J. Vac. Sci. Technol. B* **23**, 1417–1421 (2005).
34. Han, Y. *et al.* Electric-field-driven dual-functional molecular switches in tunnel junctions. *Nat. Mater.* **19**, 843–848 (2020).
35. Kawauchi, T., Oguchi, Y., Nagai, K. & Iyoda, T. Conical gradient junctions of dendritic viologen arrays on electrodes. *Sci. Rep.* **5**, 11122 (2015).
36. Cen, L., Neoh, K. G. & Kang, E. T. Gold nanocrystal formation on viologen-functionalized polymeric nanospheres. *Adv. Mater.* **17**, 1656–1661 (2005).
37. Tang, X., Schneider, T. W., Walker, J. W. & Buttry, D. A. Dimerized π-complexes in self-assembled monolayers containing viologens: An origin of unusual wave shapes in the voltammetry of monolayers. *Langmuir* **12**, 5921–5933 (1996).